Research in Astronomy and Astrophysics, 25:105013 (10pp), 2025 October
https://doi.org/10.1088/1674-4527/adf9da
CSTR: 32081.14.RAA.adf9da
© 2025. National Astronomical Observatories, CAS and IOP Publishing Ltd. All rights, including for text and data mining, AI training, and similar technologies, are reserved.

UV Flux Variation Study in Contact Binary VW Cephei

Anurag Baruah and Mayukh Pahari
Department of Physics, Indian Institute of Technology Hyderabad, Kandi, Sangareddy 502284, India; ph24resch11002@iith.ac.in
Received 2025 June 26; accepted 2025 August 1; published 2025 September 9

Abstract

Despite many attempts, the origin of UV emission line and continuum in contact binary stars remains unclear. We present a substantial UV spectroscopic analysis of VW Cephei, a late-type contact binary system, using 46 low-resolution spectra from the International Ultraviolet Explorer in the wavelength range 1150–1978 Å. By modeling continuum and emissions lines in individual spectra, we report the significant detection of O III] (1660 and 1666 Å) and Si IV (1393 and 1402 Å) line complexes. We observe that UV fluxes for both continuum and emission lines like C IV, O III], C II and Si IV vary significantly (fractional rms variability up to 45%) from hours to years. In addition, line widths also change by hundreds of km s^{-1}. The UV flux variabilities observed in the continuum bands and line emissions are uncorrelated. However, most of the flux values follow the binary orbital period observed from optical data. Our analysis indicates that, while the variation in continuum flux may be attributed to a heated photosphere, the line width measurements indicate that the emission lines are likely formed in the dynamical clouds associated with Roche lobe overflow. We estimate the mass transfer rate of $\dot{M} = (0.82 \pm 0.01) \times 10^{-7} M_{\odot}$ yr^{-1} from UV line fluxes, which is in good agreement with optical studies.

Key words: techniques: spectroscopic – (stars:) binaries: eclipsing – ultraviolet: stars

1. Introduction

Contact binaries consist of two main-sequence stars rotating around a common center of mass, in which both components fill their Roche lobes (Kopal 1959). In such systems, energy is transferred from one star to the other through the inner Lagrangian point (L1), causing the two components to share a common envelope (CE) and to have nearly equal temperatures even though their masses are quite different (Lucy 1968a, 1968b). They show continuous flux variation in their light curve. The orbital periods of most of these binaries are shorter than one day, and they follow the famous period-color relation (Eggen 1967; Rucinski 1998).

Contact binaries are divided into two main subtypes: the A-type (or early type), consisting of A or F stars and the W-type (or late type), made of G or K stars. The standard definition says that for A-type binaries, the primary minimum of eclipse is a transit. The more massive primary component has a higher surface brightness than the secondary one. In the case of W-type systems, the primary minimum corresponds to an occultation. Therefore, the secondary component has a higher mass than the primary, even though the primary has a higher temperature. These distinct physical processes in contact binaries make them a fascinating category of binary systems; studying these systems can enhance our understanding of binary star evolution and potentially contribute to broader theories of stellar evolution.

Many contact binaries show cyclic modulation, which may be due to a distant third component. Applegate (1992) proposed a mechanism that could be responsible for such cyclic period variations. According to his model, magnetic activity and cyclic variation of internal angular momentum change the gravitational quadrupole moment of the components, which in turn change the orbital period. Some contact binaries exhibit asymmetry in their light curve maxima, known as the O'Connell effect (O'Connell 1951; Milone 1968), which is likely caused by starspots resulting from magnetic activity on the stellar surfaces. The variation between the maxima can fluctuate from one orbit to the next due to the dynamic nature and evolving distribution of these cooler active regions.

VW Cephei, one of the most frequently observed contact binaries, was discovered by Schilt (1926). Its brightness ($V = 7.30$–7.84 mag) and short orbital period (~6.67 hr) make it an attractive target. The system is notable for exhibiting the O'Connell effect and for hosting a third component confirmed through astrometry (Hershey 1975). Despite extensive study, no model has yet fully accounted for all its observed properties. The unusual light curve behavior of VW Cephei was first detected during dedicated photometric monitoring by Kwee (1966). Over the years, various models have been proposed to explain its asymmetric maxima, including a circumstellar ring (Kwee 1966), a hot spot formed by gas streams (van't Veer 1973; Pustylnik & Sorgsepp 1976), precession of the stars' rotational axes (Walter 1983), and

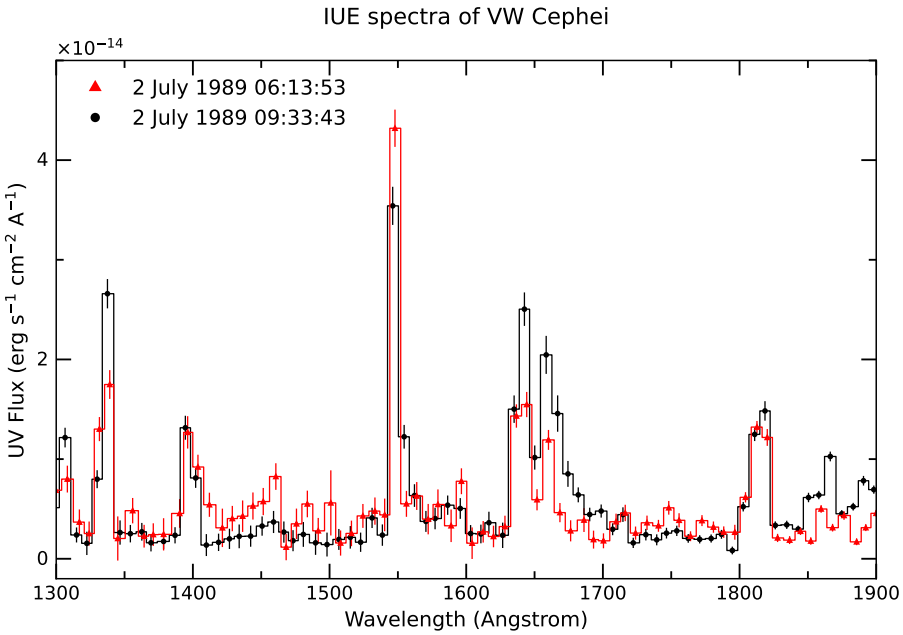


Figure 1. UV variability of VW Cephei as observed on 1989 July 2 at 06:13:53 (triangles) and 1989 July 2 at 09:33:43 (circles). For better visibility of continuum and line flux variations in short timescales, IUE spectra are plotted after binning to a coarse resolution (11.8 Å) in the wavelength range of 1300–1900 Å.

cool starspots (Yamasaki 1982). Among these, the cool starspot model has been the most consistent with observations and widely adopted in light curve modeling. Some basic information on VW Cephei is presented in Table 1.

Through optical spectroscopic analysis of VW Cephei, Hendry & Mochnacki (2000) determined a mass ratio of $q = 0.395 \pm 0.016$. Their observations also revealed that both stellar components were heavily spotted, with the more massive primary exhibiting an off-center polar spot during the time of study. X-ray spectroscopic studies of VW Cephei by Gondoin (2004) and Huenemoerder et al. (2006) revealed significant stellar activity. Gondoin (2004) found that the system possesses an extended corona enveloping both components and displays flaring behavior. Huenemoerder et al. (2006) confirmed the presence of flares and observed that the corona is predominantly concentrated near the polar regions of the primary star. In the ultraviolet (UV) regime, Sanad & Bobrowsky (2014) analyzed emission lines and detected both short- and long-term variability in their strength, which they attributed to chromospheric activity associated with the primary component. Using International Ultraviolet Explorer (IUE)/LWP data, Vilhu & Heise (1986) found the UV continuum flux of VW Cephei follows the trend of its optical data. This paper presents a detailed UV spectroscopic analysis of VW Cephei at short wavelengths and examines its continuum and emission line flux variation using the IUE data. The Si IV and O III] emission lines are detected and analyzed for the first time in this study. The observations and data reduction methods are presented in Section 2. Section 3 outlines the results obtained from the spectral analysis. In Section 4, the activity of VW Cephei based on the results is discussed. Finally, concluding remarks about this work are presented in Section 5.

Table 1
Basic Information on VW Cephei

Parameter	Value
R.A.	$20^h37^m21\overset{s}{.}63$
decl.	$+75^d36^m01\overset{s}{.}89$
Spectral type	G8V+K0V
Mass-ratio	0.302 ± 0.007
Inclination (°)	62.86 ± 0.04
Separation (a) [10^6 km]	1.412 ± 0.01

Note. Values of R.A. and decl. are taken from Gaia Collaboration et al. (2021) and all the other parameter values are from Mitnyan et al. (2018).

2. Observations and Data Reduction

IUE performed 46 low-resolution short-wavelength spectral observations between 1978 July 10 and 1992 May 30, in the wavelength range of 1150–1978 Å. We follow the data analysis methodology outlined by Wanders et al. (1997). Raw spectral images are processed using both the TOMSIPS (Ayres 1993) and NEWSIPS (Garhart et al. 1997) pipelines. For this study, we utilize the NEWSIPS-reduced spectra, in accordance with the recommendation of Wanders et al. (1997), as the TOMSIPS reduction is affected by nonlinearities in

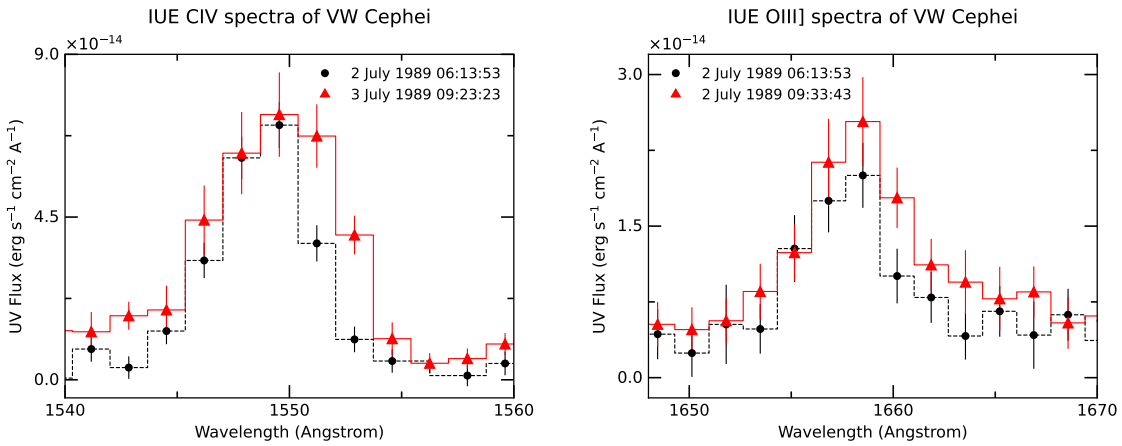


Figure 2. UV line width variability of VW Cephei. Left: Width of C IV line as observed on 1989 July 3 at 09:23:23 is broader than that of 1989 July 2 at 06:13:53. Right: Width of O III] line as observed on 1989 July 2 at 09:33:43 is broader than that of 1989 July 2 at 06:13:53.

Table 2
IUE Observations of VW Cephei

Data ID	Obs Start Time (YYYY-MM-DD HH:MM:SS)	Exp Time (s)	Data ID	Obs Start Time (YYYY-MM-DD HH:MM:SS)	Exp Time (s)
SWP01958	1978-07-10 12:38:00	3600	SWP36606	1989-07-03 07:20:08	4800
SWP02005	1978-07-14 08:27:00	9000	SWP36607	1989-07-03 09:23:23	5400
SWP06534	1979-09-16 09:11:24	9000	SWP36608	1989-07-03 12:36:18	6000
SWP06535	1979-09-16 14:39:03	2760	SWP36609	1989-07-03 15:32:25	6600
SWP07866	1980-02-04 15:32:11	3600	SWP42527	1991-09-21 07:54:56	5400
SWP07867	1980-02-04 17:05:47	3600	SWP42528	1991-09-21 10:30:03	5400
SWP30714	1987-04-05 11:50:02	6900	SWP42531	1991-09-22 01:47:07	5400
SWP30715	1987-04-05 14:59:53	5100	SWP42532	1991-09-22 05:05:04	5400
SWP33921	1988-07-15 03:42:33	4800	SWP42533	1991-09-22 07:30:06	5400
SWP33922	1988-07-15 05:48:35	4500	SWP42534	1991-09-22 10:07:12	5400
SWP33923	1988-07-15 07:47:31	4800	SWP42535	1991-09-22 12:36:43	5400
SWP33924	1988-07-15 11:22:58	4800	SWP42544	1991-09-24 02:24:45	4200
SWP33926	1988-07-15 15:44:39	5340	SWP42545	1991-09-24 05:36:37	5400
SWP36598	1989-07-02 06:13:53	3300	SWP42546	1991-09-24 09:52:15	5400
SWP36599	1989-07-02 09:33:43	6600	SWP44811	1992-05-30 07:33:25	4200
SWP36600	1989-07-02 12:22:53	6600	SWP44812	1992-05-30 10:27:07	6480
SWP36601	1989-07-02 15:46:33	6600	SWP44813	1992-05-30 13:23:43	5100
SWP36605	1989-07-03 04:47:01	5100	⋯	⋯	⋯

wavelength calibration caused by uncorrected long-term drifts. The NEWSIPS pipeline, by contrast, yields spectra that are consistent with HST observations and does not require further calibration. Notably, the NEWSIPS pipeline introduces a minor wavelength shift of about 1–2 Å due to pointing inaccuracies with the large aperture (Wanders et al. 1997). To address this, an offset correction is applied to align the prominent C IV emission line consistently across all spectra. The CCM89 (Cardelli et al. 1989) model is used for extinction corrections. Due to the very low interstellar reddening $E(B-V) = 0.0025$, corrections are not significant.

Table 2 lists the IUE observations of VW Cephei. Each spectrum was carefully examined within the 1279–1797 Å wavelength range to screen for excessive noise, overexposure, or underexposure. Based on signal-to-noise considerations, only 35 of the 46 observations are found to be of sufficient quality for reliable spectral fitting.

3. UV Spectral Analysis of VW Cephei

There is significant variability in both line and continuum flux levels, along with line widths, for IUE UV spectra. We have presented such an example in Figure 1, where the flux observed on 1989 July 2 at 06:13:53 is notably different from that recorded just three hours later.

Similarly, in Figure 2 we can see that the width of C IV as observed on 1989 July 3 at 09:23:23 is broader than that of

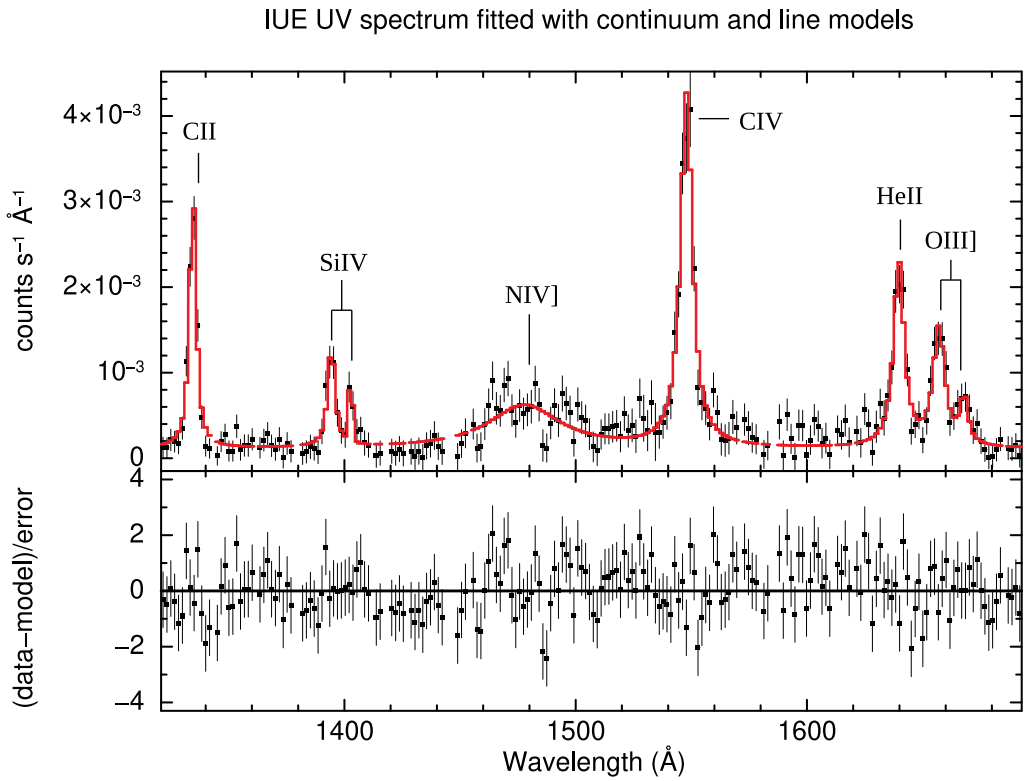


Figure 3. The best-fit (χ^2/d.o.f. = 172.45/177) UV spectrum (1320–1690 Å) is shown for the Obs ID SWP02005. The best-fit model (red) consists of continuum and emission line features, and the residual of the fitting is shown in the bottom panel. A similar fitting procedure is applied to all individual UV spectra.

1989 July 2 at 06:13:53. Likewise, the width of O III] line as observed on 1989 July 2 at 09:33:43 is broader than that of 1989 July 2 at 06:13:53.

To extract the UV continuum and line light curves from the spectra, we employ a χ^2 minimization technique using XSPEC. To enhance the signal-to-noise ratio, we bin the spectra by combining every two consecutive wavelength points. Each spectrum is fitted with a suitable combination of a power-law function–representing the underlying continuum–and multiple narrow and broad Lorentzian components to model the emission lines. The best-fitting model for the observation SPW02005 yields residuals with a reduced chi-square value of χ^2/d.o.f. = 172.45/177. The time-averaged UV spectrum along with the model components and residuals is shown in Figure 3, and the corresponding best-fit parameters are listed in Table 3. From the best-fitting model, the integrated fluxes of emission lines and the UV continuum are computed using the CFLUX convolution model in XSPEC, which provides both the flux values over a specified wavelength range and their associated 1σ uncertainties. We calculated the continuum flux in the range 1343–1390 Å (CONT1) and 1565–1633 Å (CONT2) and line fluxes at 1336 (C II), 1393 (Si IV), 1550 (C IV) and 1660 (O III]) Å. Each of 35 spectra is fitted separately with the best-fitting model to obtain the continuum and line fluxes from each pointing.

Figure 4 presents the variation of UV continuum and emission line flux with time, revealing significant variability in both components. Corresponding values are given in Table 4. For better visibility and to enable comparison with the optical light curve, we have shown the UV flux for observations of the year 1989 alongside the corresponding optical magnitudes from the same period in Figure 5. The optical data are taken from Kreiner & Winiarski (1981) and extrapolated to our required timescale using a period of 6.67 hr.

In Table 5, we present the average flux, standard deviation (SD), rms and fractional rms for each continuum and emission line light curve. The rms and fractional rms are calculated using the standard formulas as defined in the following equations, where x_i denotes the individual flux measurements and σ_i represents the corresponding flux uncertainties. N is the total number of flux data points.

$$\mathrm{rms} = \sqrt{\frac{1}{N}\sum_{i=1}^{N} x_i^2}, \quad F_{\mathrm{rms}} = \frac{\sqrt{\mathrm{SD}^2 - \langle \sigma_i^2 \rangle}}{\langle x \rangle}.$$

The relatively large SD values across all light curves indicate substantial variability in both the UV continuum and emission lines. Furthermore, high fractional rms values signify that the amplitude of variability is comparable to the average flux level, reflecting strong intrinsic fluctuations in the source.

Table 3
Best Fit Parameters for the IUE Spectra of VW Cephei on 1978 July 14 at 08:27:00 (SWP02005)

Emission Line	Component	Parameter	Value
C IV	lorentz	LineE (10^{-3} keV)	8.01 ± 0.01
		Width (10^{-5} keV)	$3.05^{+0.28}_{-0.19}$
		norm	0.04 ± 0.02
C II	lorentz	LineE (10^{-3} keV)	9.29 ± 0.01
		Width (10^{-5} keV)	$2.14^{+0.15}_{-0.23}$
		norm	0.02 ± 0.01
Si IV[1]	lorentz	LineE (10^{-3} keV)	8.89 ± 0.03
		Width (10^{-5} keV)	$2.15^{+0.45}_{-0.33}$
		norm	0.01 ± 0.01
Si IV[2]	lorentz	LineE (10^{-3} keV)	$8.83^{+0.06}_{-0.03}$
		Width (10^{-4} keV)	$2.25^{+0.08}_{-0.02}$
		norm	0.01 ± 0.01
He II	lorentz	LineE (10^{-3} keV)	7.56 ± 0.01
		Width (10^{-5} keV)	$2.39^{+0.35}_{-0.14}$
		norm	0.02 ± 0.01
O III][1]	lorentz	LineE (10^{-3} keV)	$7.48^{+0.13}_{-0.19}$
		Width (10^{-5} keV)	2.61 ± 0.28
		norm	0.01 ± 0.01
O III][2]	lorentz	LineE (10^{-3} keV)	7.43 ± 0.03
		Width (10^{-5} keV)	$1.67^{+0.74}_{-0.41}$
		norm	0.03 ± 0.01
N IV]	lorentz	LineE (10^{-3} keV)	8.36 ± 0.01
		Width (10^{-4} keV)	2.13 ± 0.25
		norm	0.03 ± 0.02
	powerlaw	PhoIndex	1.93 ± 0.03
		norm	0.02 ± 0.01

Our analysis also shows that there is noteworthy variation in width of emission lines. This temporal variation of line width is calculated for C IV, C II, Si IV and O III] lines and plotted for C IV and O III] lines in Figures 6 and 7 respectively. Corresponding values of velocity widths due to Doppler broadening, for 1989 July 2–3, are calculated using the relation $\Delta v = \frac{\Delta\lambda}{\lambda}.c$ and presented in Table 6.

To investigate any potential correlation between the continuum flux and the line fluxes, we computed the Spearman rank, Pearson, and Kendall tau correlation coefficients, along with their associated p-values for various combinations of UV fluxes. These results are summarized in Table 7, with the corresponding correlation plot shown in Figure 8. We have not numerically correlated UV fluxes with optical magnitude as we do not have simultaneous observation data. For visualization, though we have extrapolated the optical light curve with a 6.67 hr period, it is not entirely accurate as the period is continuously decreasing in the order of 10^{-7} days yr^{-1} (Mitnyan et al. 2018).

4. Discussion

UV line emission of contact binaries is generally attributed to its chromospheric behavior. IUE chromospheric lines have a temperature of 10^4 K and transition region lines indicate a temperature of 10^5 K from hot plasma (Vilhu & Heise 1986). VW Cephei, because of its rapid rotation and enhanced dynamo activity, shows variation of flux in near and far UV. According to Dupree et al. (1980), the continuum emission is primarily due to heated photosphere and transition region activity. While the effective surface temperatures of the primary and secondary components are about 5050 and 5342 K, respectively (Mitnyan et al. 2018), which would typically produce a weak UV continuum, our spectral analysis shows that the UV continuum can be described by a power-law, which indicates that the origin of UV emission may include a combination of hot, optically thin plasma in the chromosphere and transition region, where temperatures exceed the photospheric values. In general, the C IV line at 1550 Å, Si IV line at 1393 Å and C II line at 1336 Å are resonance lines formed under collisionally dominated conditions, which originate in the highly active outer atmospheres. In contrast, the O III] line at 1660 Å is a semi-forbidden transition, meaning this is an intercombination line, allowed only due to spin–orbit coupling. They occur in low-density, collisionally ionized regions, where the metastable upper states have time to decay radiatively. Sanad & Bobrowsky (2014) attributed this variability of line fluxes to changes in local density and temperature, which are likely influenced by the presence and evolution of magnetically active regions, particularly on the primary star. Modeling studies using PHOEBE (Prša & Zwitter 2005) further support this interpretation. Mitnyan et al. (2018) show that the starspots on VW Cephei are located on the two opposite hemispheres of the primary star, aligned with the line connecting the two components. Hence there is a correlation between spottedness and the strength of the chromospheric activity. Figure 5 is consistent with the results of Vilhu & Heise (1986); at longer wavelengths (2580–3180 Å), the UV continuum follows the general trend of the optical light curve and Sanad & Bobrowsky (2014); fluxes for emission lines exhibit a clear correlation with the optical variations.

Table 6 shows variability of velocity widths due to Doppler broadening reaching up to $\sim$1000 km s^{-1}. These values are considerably higher than the typical velocities expected from chromospheric turbulence or rotational broadening due to cool starspots. This discrepancy suggests that spot-related activity alone cannot account for the observed line broadening. Instead, the measured widths are more consistent with gas motion associated with Roche lobe overflow (RLOF). Using the system parameters of VW Cephei ($a = 1.41 \times 10^6$ km and $M_1 = 1.13 M_\odot$; Mitnyan et al. 2018), the velocity of material flowing through the inner Lagrangian point (L1) can be approximated as $\sim$652 km s^{-1}, using a simple conservation of energy equation: $v = \sqrt{\frac{2GM_1}{r}}$, where $r = a/2$ is the approximate distance from the primary to L1. Thus the

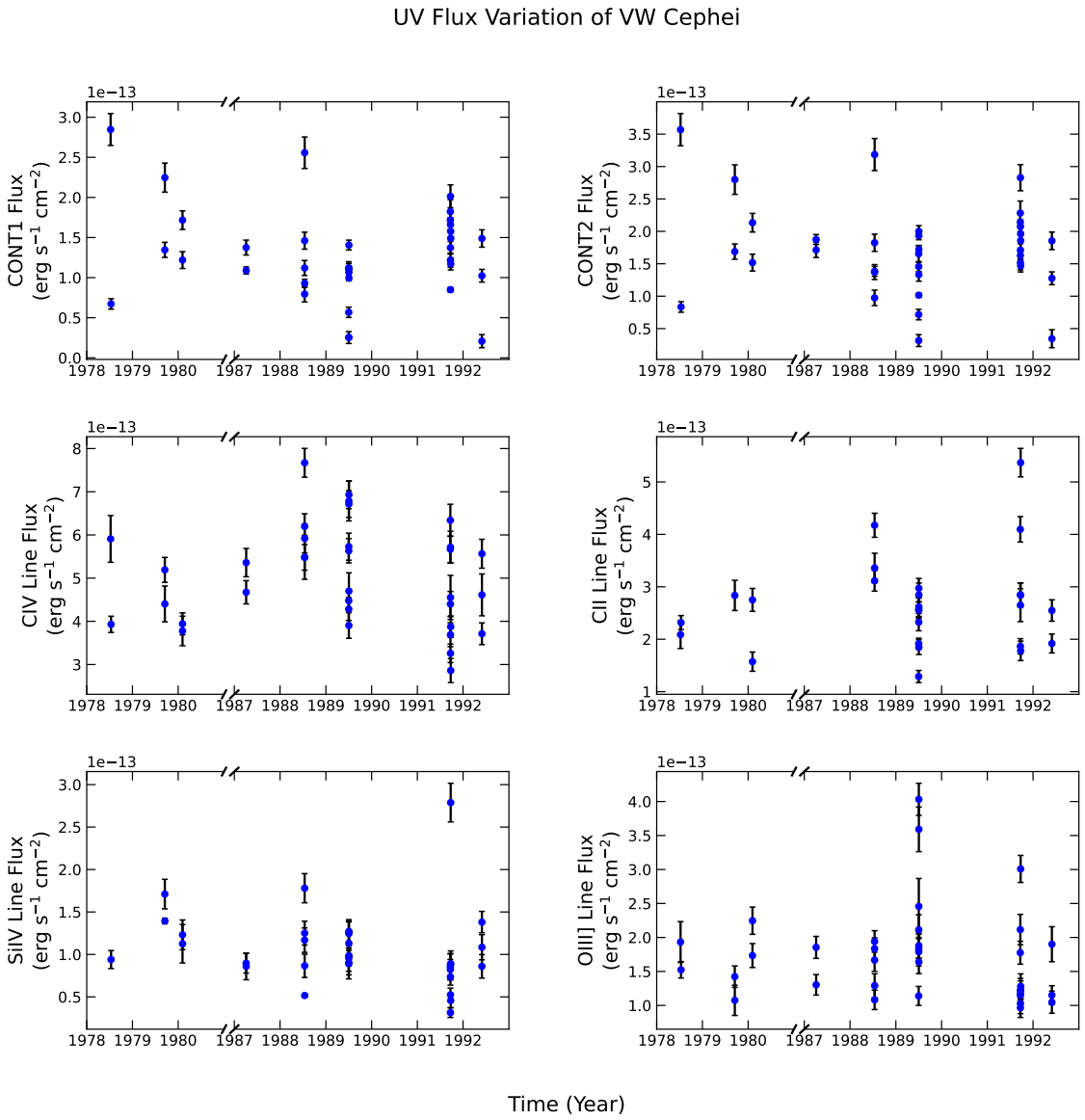


Figure 4. UV continuum, C IV, C II, Si IV and O III] line flux variation of IUE SWP data from 1978 to 1992. CONT1 and CONT2 represent the continuum flux in the range 1343–1390 Å and 1565–1633 Å respectively.

observed broadening matches well with the expected velocities from ballistic mass transfer, providing strong evidence that these UV line profiles are shaped by high-speed accretion flows rather than photospheric or chromospheric processes. Additionally, from Table 7 we conclude that the variations of line fluxes are correlated with each other, but the dependence of line and continuum with each other is statistically insignificant. This supports the interpretation that the line-emitting plasma originates in dynamically heated accretion streams, distinct from the continuum-originating photospheric or spot-dominated regions of the stars.

Using the mean flux values from Table 5, we calculate the total UV flux to be $F_{\rm UV} = (13.45 \pm 0.08) \times 10^{-13}\,{\rm erg\,s^{-1}\,cm^{-2}}$. Adopting a distance of $d = 26.54$ pc (Gaia Collaboration et al. 2021), this corresponds to a UV luminosity of $L_{\rm UV} = 4\pi d^2 F_{\rm UV} = (1.13 \pm 0.01) \times 10^{29}\,{\rm erg\,s^{-1}}$. For G-type and K-type stars, the typical bolometric correction factor in the UV is $\sim 10^{-5}$. Applying this, we estimate the bolometric luminosity, $L_{\rm Bol} = (1.13 \pm 0.01) \times 10^{34}\,{\rm erg\,s^{-1}}$. Using the standard formula for conservative mass transfer, $\dot{M} = \frac{L_{\rm Bol} R_1}{G M_1}$ and adopting $M_1 = 1.13\,M_\odot$ and $R_1 = 0.99\,R_\odot$ (Mitnyan et al. 2018), we derive a mass transfer rate of $\dot{M} = (0.82 \pm 0.01) \times 10^{-7}\,M_\odot\,{\rm yr^{-1}}$, which agrees reasonably well with the value obtained from optical light curve studies, $\dot{M}_{\rm opt} = (1.11 \pm 0.05) \times 10^{-7}\,M_\odot\,{\rm yr^{-1}}$, as reported by Mitnyan et al. (2018). Therefore, the large and variable line widths, rapid temporal modulation of UV fluxes, and weak correlation between

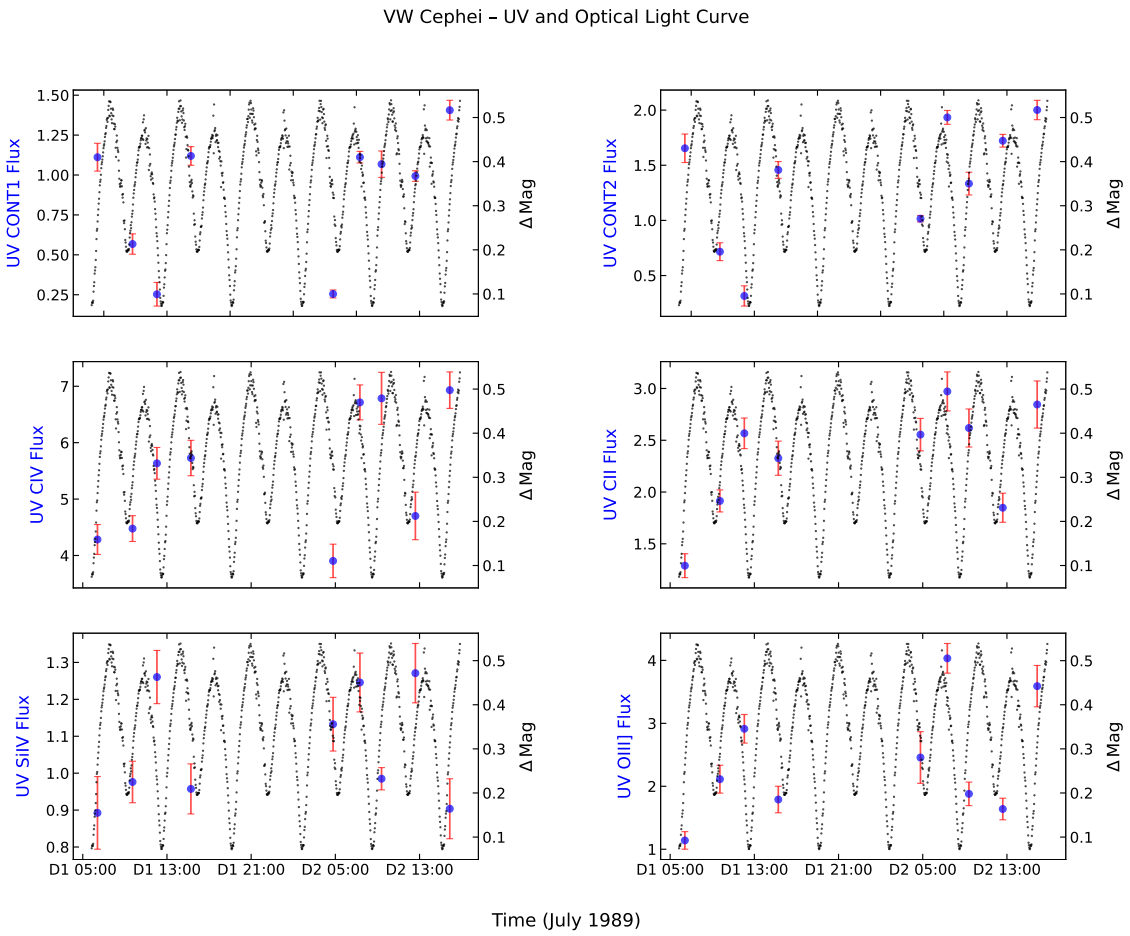


Figure 5. UV continuum and line flux variability of VW Cephei as observed in July of 1989. The flux axis has unit 10^{-13} erg s^{-1} cm^{-2}. UV flux (blue dots) is plotted alongside optical data (black dots) in ΔMag scale. The optical data are taken from Kreiner & Winiarski (1981) and extrapolated to our required timescale using a period of 6.67 hr and an epoch of HJD 2444157.4131, corresponding to the primary minimum ($E = 0$) on 1979 October 10. D1 and D2 correspond to day 1 (1989 July 2) and day 2 (1989 July 3), respectively.

Table 4
Fluxes from SWP Spectral Modeling in 10^{-13} erg s^{-1} cm^{-2} Along with Respective Reduced Chi-square Values

Data ID	CONT1 Flux	CONT2 Flux	C IV Flux	C II Flux	Si IV Flux	O III] Flux	χ^2/dof
SWP01958	2.85 ± 0.20	3.57 ± 0.25	5.91 ± 0.54	2.09 ± 0.26	ND	1.93 ± 0.30	120.77/163
SWP02005	0.67 ± 0.07	0.83 ± 0.08	3.93 ± 0.19	2.32 ± 0.13	0.94 ± 0.11	1.52 ± 0.12	172.45/177
SWP06534	1.35 ± 0.09	1.69 ± 0.12	5.19 ± 0.29	0.02 ± 0.01	1.71 ± 0.17	1.42 ± 0.16	214.32/195
SWP06535	2.25 ± 0.18	2.80 ± 0.23	4.40 ± 0.42	2.84 ± 0.28	1.39 ± 0.03	1.07 ± 0.22	148.34/149
SWP07866	1.22 ± 0.10	1.52 ± 0.13	3.78 ± 0.34	1.57 ± 0.18	1.13 ± 0.23	1.73 ± 0.18	112.32/176
SWP07867	1.72 ± 0.12	2.13 ± 0.14	3.94 ± 0.25	2.75 ± 0.21	1.23 ± 0.17	2.25 ± 0.20	174.44/183
SWP30714	1.37 ± 0.09	1.71 ± 0.12	4.67 ± 0.27	0.02 ± 0.01	0.90 ± 0.12	1.85 ± 0.16	178.09/175
SWP30715	1.09 ± 0.04	1.87 ± 0.08	5.36 ± 0.33	0.02 ± 0.02	0.86 ± 0.16	1.30 ± 0.15	266.30/163
SWP33921	1.12 ± 0.09	1.37 ± 0.12	6.20 ± 0.29	3.11 ± 0.19	1.17 ± 0.14	1.94 ± 0.16	179.07/164
SWP33922	0.79 ± 0.10	0.97 ± 0.12	7.67 ± 0.33	4.17 ± 0.23	1.25 ± 0.14	1.84 ± 0.16	183.19/183
SWP33923	1.46 ± 0.11	1.82 ± 0.13	5.48 ± 0.29	0.03 ± 0.02	1.78 ± 0.17	1.67 ± 0.17	172.61/169
SWP33924	0.93 ± 0.05	1.38 ± 0.08	5.92 ± 0.34	0.02 ± 0.01	0.87 ± 0.14	1.08 ± 0.14	161.94/173
SWP33926	2.56 ± 0.20	3.18 ± 0.25	5.48 ± 0.51	3.36 ± 0.28	0.52 ± 0.02	1.29 ± 0.18	122.67/159
SWP36598	1.11 ± 0.09	1.65 ± 0.13	4.28 ± 0.26	1.29 ± 0.16	0.89 ± 0.18	1.14 ± 0.14	135.28/172
SWP36599	0.57 ± 0.06	0.72 ± 0.08	4.48 ± 0.22	1.91 ± 0.11	0.98 ± 0.10	2.11 ± 0.22	212.35/177
SWP36600	0.25 ± 0.07	0.32 ± 0.09	5.63 ± 0.28	2.57 ± 0.15	1.26 ± 0.13	2.92 ± 0.14	217.09/172

Table 4
(Continued)

Data ID	CONT1 Flux	CONT2 Flux	C IV Flux	C II Flux	Si IV Flux	O III] Flux	χ^2/dof
SWP36601	1.12 ± 0.06	1.46 ± 0.08	5.73 ± 0.31	2.33 ± 0.16	0.96 ± 0.16	1.79 ± 0.21	232.11/146
SWP36605	0.25 ± 0.01	1.02 ± 0.03	3.90 ± 0.29	2.55 ± 0.16	1.13 ± 0.12	2.46 ± 0.41	177.73/173
SWP36606	1.11 ± 0.04	1.93 ± 0.06	6.71 ± 0.31	2.97 ± 0.18	1.25 ± 0.14	4.03 ± 0.24	279.14/175
SWP36607	1.07 ± 0.08	1.33 ± 0.10	6.79 ± 0.46	2.62 ± 0.18	0.98 ± 0.12	1.88 ± 0.19	220.30/173
SWP36608	0.99 ± 0.03	1.72 ± 0.06	4.70 ± 0.42	1.85 ± 0.14	1.27 ± 0.14	1.64 ± 0.17	262.57/173
SWP36609	1.41 ± 0.06	2.00 ± 0.09	6.93 ± 0.32	2.85 ± 0.23	0.90 ± 0.14	3.59 ± 0.33	262.92/162
SWP42527	1.72 ± 0.12	2.14 ± 0.15	5.67 ± 0.31	4.10 ± 0.24	0.82 ± 0.12	1.78 ± 0.17	214.44/167
SWP42528	1.82 ± 0.15	2.28 ± 0.19	6.34 ± 0.37	2.85 ± 0.22	0.85 ± 0.15	2.12 ± 0.22	125.65/164
SWP42531	0.85 ± 0.03	1.63 ± 0.05	4.40 ± 0.29	1.87 ± 0.15	0.31 ± 0.06	1.17 ± 0.11	167.56/169
SWP42532	1.37 ± 0.08	1.71 ± 0.10	3.69 ± 0.27	0.03 ± 0.02	0.73 ± 0.10	1.15 ± 0.12	234.87/171
SWP42533	1.22 ± 0.09	1.52 ± 0.11	3.26 ± 0.22	0.03 ± 0.02	0.52 ± 0.08	0.96 ± 0.14	207.21/164
SWP42534	2.01 ± 0.14	2.83 ± 0.20	5.72 ± 0.37	2.65 ± 0.32	ND	1.22 ± 0.17	128.77/172
SWP42535	1.66 ± 0.09	2.07 ± 0.11	4.55 ± 0.51	0.02 ± 0.01	0.88 ± 0.13	1.03 ± 0.15	230.96/183
SWP42544	1.58 ± 0.10	1.96 ± 0.13	3.86 ± 0.25	5.37 ± 0.27	2.79 ± 0.23	3.01 ± 0.20	255.95/194
SWP42545	1.17 ± 0.08	1.47 ± 0.09	3.88 ± 0.25	1.78 ± 0.18	0.46 ± 0.08	1.22 ± 0.14	150.14/188
SWP42546	1.49 ± 0.10	1.86 ± 0.13	2.86 ± 0.28	2.84 ± 0.23	0.89 ± 0.15	1.28 ± 0.18	179.31/176
SWP44811	0.21 ± 0.08	0.34 ± 0.14	5.56 ± 0.33	0.03 ± 0.01	0.86 ± 0.14	1.15 ± 0.14	182.59/170
SWP44812	1.02 ± 0.08	1.28 ± 0.10	3.71 ± 0.25	2.55 ± 0.20	1.38 ± 0.13	1.05 ± 0.16	235.45/189
SWP44813	1.49 ± 0.11	1.85 ± 0.14	4.61 ± 0.48	1.92 ± 0.18	1.08 ± 0.15	1.90 ± 0.26	162.17/168

Note. Continuum fluxes are calculated within the wavelength range of 1343–1390 Å (CONT1) and 1565–1633 Å (CONT2). ND: Not Detected.

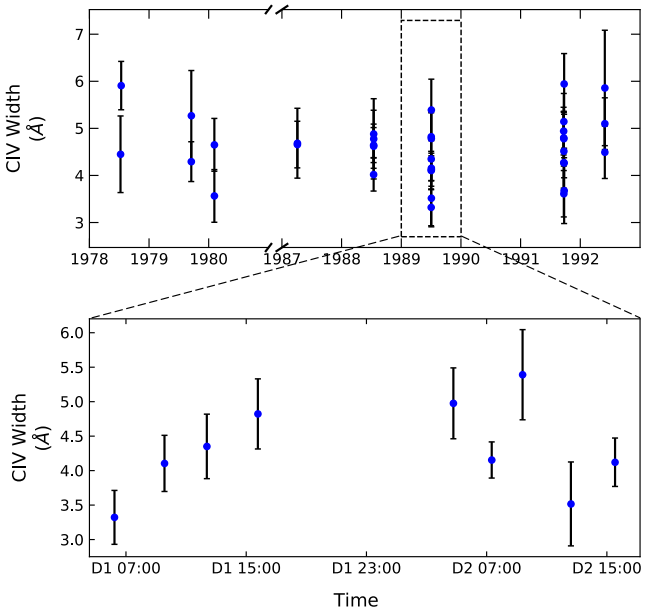


Figure 6. Variation of C IV line width over time. Top: Long-term variation (over years). Bottom: Short-term variation. D1 and D2 correspond to day 1 (1989 July 2) and day 2 (1989 July 3), respectively.

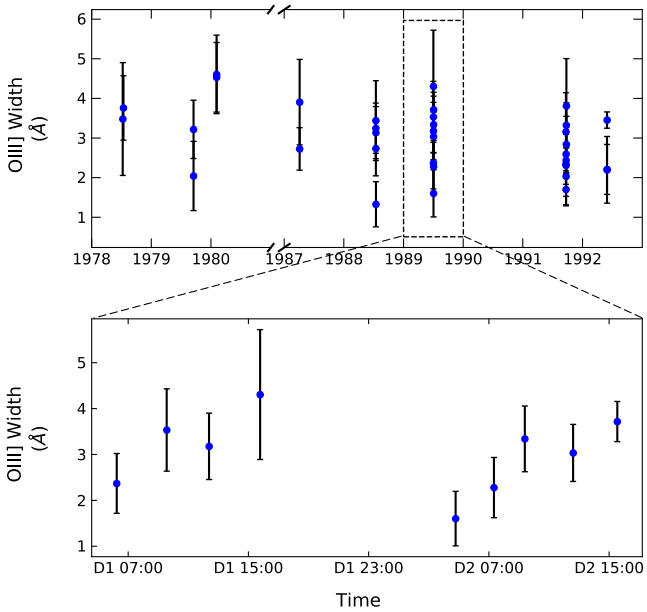


Figure 7. Variation of O III] line width over time. Top: Long-term variation (over years). Bottom: Short-term variation. D1 and D2 correspond to day 1 (1989 July 2) and day 2 (1989 July 3), respectively.

line and continuum fluxes support the interpretation that the UV line profiles in VW Cephei are shaped by high velocity gas flows originating from RLOF. The variability in line broadening likely reflects changes in the accretion stream geometry, impact conditions, or density fluctuations within the flow as the system evolves over the orbital cycle. However, to fully disentangle the physical origins of both the line and continuum emission, and to understand their variability, future simultaneous multiwavelength observations will be essential.

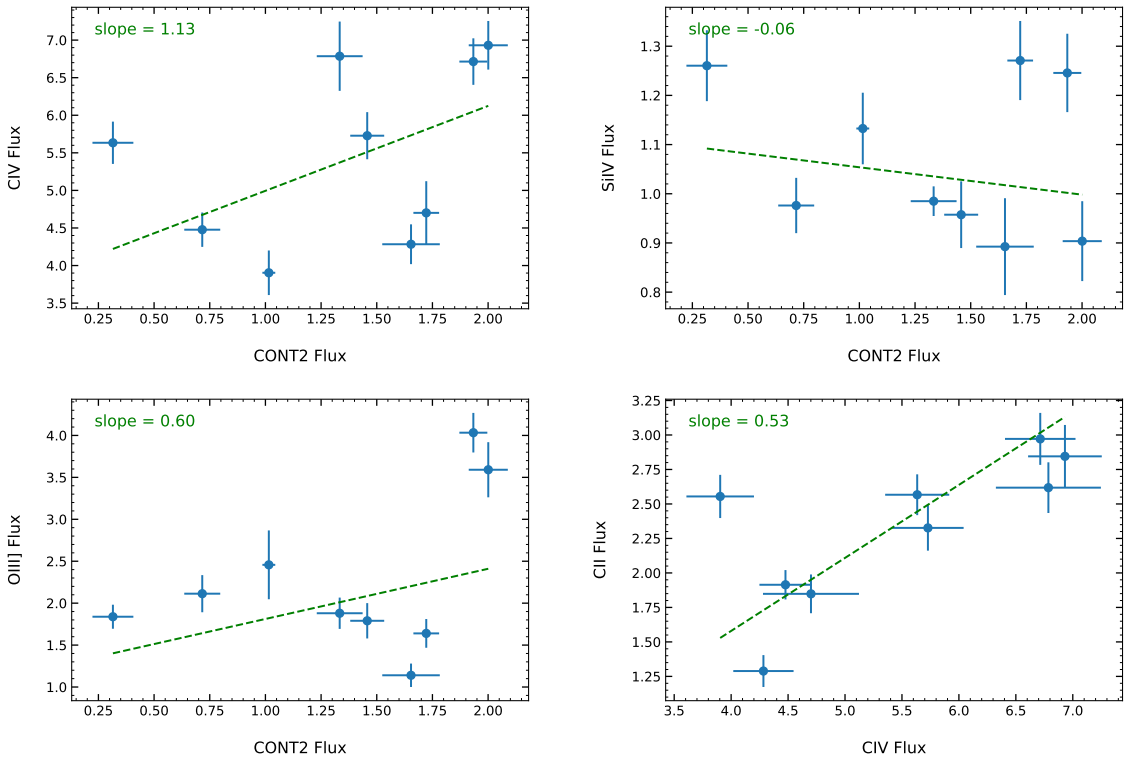


Figure 8. Correlation between UV continuum (CONT2: 1565–1633 Å) and line fluxes (10^{-13} erg s^{-1} cm^{-2}).

Table 5
Mean Flux, Standard Deviation (SD), rms and Fractional rms for the Continuum and Emission Line Light Curves

Light Curve Type	Mean Flux	Standard Deviation	rms	Fractional rms
CONT1	1.28 ± 0.02	0.59 ± 0.07	1.41 ± 0.02	45 ± 6%
CONT2	1.71 ± 0.02	0.70 ± 0.08	1.85 ± 0.03	40 ± 5%
C IV	5.01 ± 0.06	1.15 ± 0.14	5.13 ± 0.06	22 ± 3%
C II	2.66 ± 0.04	0.88 ± 0.12	2.79 ± 0.04	32% ± 5%
Si IV	1.06 ± 0.02	0.45 ± 0.06	1.15 ± 0.03	39% ± 4%
O III]	1.73 ± 0.03	0.70 ± 0.08	1.86 ± 0.04	38% ± 5%

Note. The flux, SD, and rms values are expressed in units of 10^{-13} erg s^{-1} cm^{-2}.

Table 6
C IV, C II, Si IV and O III] Velocity Widths Due to Doppler Broadening for Observations on 1989 July 2–3

Observation ID	C IV Velocity Width (km s^{-1})	C II Velocity Width (km s^{-1})	Si IV Velocity Width (km s^{-1})	O III] Velocity Width (km s^{-1})
SWP36598	642.95 ± 75.66	593.26 ± 113.71	770.27 ± 91.67	661.07 ± 181.86
SWP36599	794.43 ± 78.87	643.55 ± 74.37	587.28 ± 157.84	986.04 ± 250.37
SWP36600	842.16 ± 90.55	857.87 ± 99.09	899.46 ± 238.83	886.62 ± 201.75
SWP36601	933.40 ± 98.40	879.72 ± 133.33	820.15 ± 339.35	1201.49 ± 394.82
SWP36605	963.10 ± 99.53	908.78 ± 139.03	253.80 ± 107.79	447.23 ± 165.73
SWP36606	804.01 ± 50.74	682.09 ± 64.59	438.21 ± 90.39	635.81 ± 183.22
SWP36607	1043.43 ± 126.53	796.83 ± 123.93	518.70 ± 142.60	932.14 ± 199.80
SWP36608	680.67 ± 117.76	688.09 ± 119.28	695.74 ± 250.72	846.72 ± 173.55
SWP36609	797.71 ± 67.96	741.47 ± 116.50	545.78 ± 178.21	1037.48 ± 122.03

Table 7
Correlation Coefficients with their *p*-values for Different Combinations of Continuum (CONT1: 1343–1390 Å, CONT2: 1565–1633 Å) and Line Fluxes

Flux Combination	Pearson r	*p*-value	Spearman rho	*p*-value	Kendall tau	*p*-value
CONT1 - C IV	0.565	0.113	0.617	0.077	0.444	0.119
CONT1 - Si IV	−0.454	0.220	−0.583	0.099	−0.444	0.119
CONT1 - O III]	0.251	0.515	0.150	0.700	0.056	0.919
CONT2 - C IV	0.379	0.314	0.467	0.205	0.333	0.260
CONT2 - Si IV	−0.214	0.580	−0.217	0.576	0.222	0.477
CONT2 - O III]	0.406	0.278	0.183	0.637	0.056	0.919
C IV - C II	0.716	0.030	0.733	0.025	0.556	0.045

5. Conclusion

A detailed spectroscopic investigation of the UV emission from the contact binary VW Cephei has been carried out using archival short-wavelength prime data from the IUE. The analysis reveals prominent emission lines from ionized metal species, notably C II and C IV, which are characteristic of late-type contact binaries. Emission lines due to O III] and Si IV have also been reported for the first time for VW Cephei from our analysis. The UV flux variation appears to follow a similar trend to that observed in the optical light curves, suggesting a correlation between magnetic activity and UV variability. Rapid variability is observed in UV continuum (fractional rms of 40%–45%) as well as UV line fluxes (22%–42%) and they seem uncorrelated. This may imply that the line and continuum may have different geometric origins. However, simultaneous multi-wavelength observations are required for better understanding of the RLOF geometry in VW Cephei. The change in velocity width of the line-emitting gas clouds is probably due to mass transfer between the binary components. To better understand the physical processes responsible for the emission features, especially the temporal behavior of the lines, additional multi-epoch UV observations are necessary.

Acknowledgments

A.B. acknowledges DST, Government of India for the award of INSPIRE fellowship (IF230384) and the research facility of Department of Physics, IIT Hyderabad.

ORCID iDs

Anurag Baruah https://orcid.org/0009-0005-4311-0810
Mayukh Pahari https://orcid.org/0000-0002-5900-9785

References

Applegate, J. H. 1992, ApJ, 385, 621
Ayres, T. R. 1993, PASP, 105, 538
Cardelli, J. A., Clayton, G. C., & Mathis, J. S. 1989, ApJ, 345, 245
Dupree, A. K., Hartmann, L., & Raymond, J. C. 1980, in IAU Symp. 88, Close Binary Stars: Observations and Interpretation, ed. M. J. Plavec, D. M. Popper, & R. K. Ulrich (Cambridge: Cambridge Univ. Press), 39
Eggen, O. J. 1967, MmRAS, 70, 111
Gaia Collaboration, Brown, A. G. A., Vallenari, A., et al. 2021, A&A, 649, A1
Garhart, M. P., Smith, M. A., Turnrose, B. E., Levay, K. L., & Thompson, R. W. 1997, IUE NASA Newsletter, 57, 1
Gondoin, P. 2004, A&A, 415, 1113
Hendry, P. D., & Mochnacki, S. W. 2000, ApJ, 531, 467
Hershey, J. L. 1975, AJ, 80, 662
Huenemoerder, D. P., Testa, P., & Buzasi, D. L. 2006, ApJ, 650, 1119
Kopal, Z. 1959, Close Binary Systems (The International Astrophysics Series, London: Chapman & Hall)
Kreiner, J. M., & Winiarski, M. 1981, AcA, 31, 351
Kwee, K. K. 1966, BAN, 18, 448
Lucy, L. B. 1968a, ApJ, 153, 877
Lucy, L. B. 1968b, ApJ, 151, 1123
Milone, E. F. 1968, AJS, 73, 26
Mitnyan, T., Bódi, A., Szalai, T., et al. 2018, A&A, 612, A91
O'Connell, D. J. K. 1951, PRCO, 2, 85
Prša, A., & Zwitter, T. 2005, ApJ, 628, 426
Pustylnik, I., & Sorgsepp, L. 1976, AcA, 26, 319
Rucinski, S. M. 1998, AJ, 116, 2998
Sanad, M. R., & Bobrowsky, M. 2014, NewA, 29, 47
Schilt, J. 1926, ApJ, 64, 215
van't Veer, F. 1973, A&A, 26, 357
Vilhu, O., & Heise, J. 1986, ApJ, 311, 937
Walter, K. 1983, A&A, 128, 391
Wanders, I., Peterson, B. M., Alloin, D., et al. 1997, ApJS, 113, 69
Yamasaki, A. 1982, Ap&SS, 85, 43